ISSN 1063-7729, Astronomy Reports, 2012, Vol. 56, No. 1, pp. 16–28. © Pleiades Publishing, Ltd., 2012.
Original Russian Text © A.V. Khoperskov, M.A. Eremin, S.A. Khoperskov, M.A. Butenko, A.G. Morozov, 2012, published in Astronomicheskii Zhurnal, 2012, Vol. 89, No. 1, pp. 19–31.

Dynamics of Gaseous Disks in a Non-axisymmetric Dark Halo

A. V. Khoperskov*, M. A. Eremin, S. A. Khoperskov, M. A. Butenko, and A. G. Morozov

Volgograd State University, Volgograd, Russia

Received April 4, 2010; in final form, June 15, 2011

Abstract—The dynamics of a galactic disk in a non-axisymmetric (triaxial) dark halo is studied in detail using high-resolution, numerical, hydrodynamical models. A long-lived, two-armed spiral pattern is generated for a wide range of parameters. The spiral structure is global, and the number of turns can be two or three, depending on the model parameters. The morphology and kinematics of the spiral pattern are studied as functions of the halo and disk parameters. The spiral structure rotates slowly, and its angular velocity varies quasi-periodically. Models with differing relative halo masses, halo semi-axis ratios, distributions of matter in the disk, Mach numbers in the gaseous component, and angular rotational velocities of their halos are considered.

DOI: 10.1134/S1063772912010039

1. INTRODUCTION

Galactic gaseous and stellar disks are axisymmetric only in a first approximation. Spiral density waves, a central bar, the non-axisymmetry (triaxial nature) of a dark massive halo, satellite galaxies, or a triaxial bulge can disturb the axial symmetry of the "external" gravitational potential in which the galactic disk component is situated. Results of dynamic modeling of specific disk galaxies, designed to agree with photometric and kinematic data, indicate the need to take into account a dark halo of mass M_h (which exceeds the mass of the disk component M_d by a factor of one to four [1–5]) inside the optical radius of the stellar component R. The kinematics of objects in the immediate vicinity of the Milky Way–M31 pair indicate that the total mass inside 0.96 Mpc is $M_T \sim 2 \times 10^{12} M_\odot$ [6], and the ratio of the masses of the Milky Way and M31 is $M_{\rm MW}/M_{\rm M31} = 4/5$. Since the mass of the disk component of our Galaxy probably does not exceed $5 \times 10^{10} M_\odot$ [7], $\sim 15\%$ of the total mass within 1 Mpc belongs to the disk subsystems.

There is much theoretical and observational evidence indicating the absence of central symmetry in the dark-mass distribution within the disk components of S galaxies. The triaxial shape of the halo can be characterized by three space scales: a, b, c.

Studies of galaxy formation based on cosmological N-body models indicate triaxial mass distributions in cold-dark-matter (CDM) halos, with the following semi-axis ratios obtained in different studies: $s = c/a \sim 0.6$–0.7, $q = b/a \sim 0.8$–0.95 [8]; $\langle s \rangle \simeq 0.7$, $\langle q \rangle \simeq 0.8$ [9]; $\langle s \rangle \simeq 0.6$, $\langle q \rangle \simeq 0.75$ [10]. At the same time, triaxial parameters s and q depend on the halo mass, redshift, and distance to the halo center. The dark halo is more symmetrical near the center than at the periphery. The distributions turn out more symmetrical in hot-dark-matter models than in CDM models [9].

Observations of the Sagittarius tidal stream (Sagittarius dSph) indicate a lack of central symmetry of the halo, with the axial ratio $c/a \gtrsim 0.8$ [11]. However, if this stream is dynamically young, then $c/a \simeq 0.6$ is possible [12]. Arc-shaped stellar tidal streams found in the Sloan Digital Sky Survey (SDSS), apparently resulting from the absorption of dwarf galaxies, seem to be promising indicators of a dark halo. The Virgo over-density structure could be related to such peculiarities in the distribution of the observed matter in the halo [13]. Stellar tidal streams have been discovered in M31 [14] and a number of outer galaxies (e.g., NGC 5907 [15], NGC 3310 [16], NGC 1055 (see http://www.imagingdeepsky.com)). These streams are apparently connected with the disruption of dwarf galaxies in the massive triaxial halo.

Observations of stars (RR Lyr, F dwarfs) indicate a lack of central symmetry of the halo [13]. Direct kinematic observations of various halo objects (globular clusters, satellites, blue horizontal-branch stars, red giants) can be used to find the radial velocity-dispersion profile which, in turn, indicates the character of the gravitating mass distribution for a given halo model. New possibilities for deriving halo param-

*E-mail: akhoperskov@rambler.ru

eters are provided by observations of hyper-velocity stars [17–19].

Deep surveys of edge-on galaxies indicate a strong prevalence for stellar halos in the form of oblate spheroids with axial ratios of ∼0.6, which have been attributed to tidal interactions [14–20]. Cosmological models taking into account the stellar-halo dynamics also give triaxial shapes for the dark halo ($s = 0.84$, $q = 0.94$) and stellar halo ($s = 0.84$, $q = 0.91$) [21].

Several techniques for determining halo shapes (a, b, c) from observations can be identified [22], based on: (1) expansion of the HI gaseous disk with distance from the center (flaring of the gaseous layer)—other conditions being equal, the thickness of the gaseous disk decreases with increase in the degree of flattening of the halo; (2) warping of the gaseous layer; (3) X-ray isophotes; (4) outer polar rings—a dynamical model of the polar ring is constructed allowing for an asymmetric halo and fit to the observational data; and (5) the parameters of a precessing dust disk. The observational data for our Galaxy indicate that the both the stellar and dark-matter halos do not display central symmetry. Different approaches based on observations of different objects lead to estimates of $s \simeq 0.2$–0.9 (see, e.g., [23, 24]).

Thus, one of the most important properties of a halo is the triaxial character of the mass distribution in it. In turn, information on the character of the dark-matter distributions in galaxies and in their immediate vicinities, together with observations of the isotropic gamma-ray background, can be used to derive constraints on particle dark-matter models [25].

Let us consider the dynamics of a rotating gaseous disk in the non-axisymmetric gravitational field of a dark halo. Let us assume that the mass of the stellar–gaseous disk within the limits of the optical radius R is comparable to the dark mass [2, 26, 27]. The influence of the global asymmetry of the potential on the formation of dynamical structures in the disk is of the most interest. It seems natural to expect that the disk responds to this influence by forming a spiral pattern [28, 29].

Let us consider the hypothesis that the non-axisymmetry (triaxial nature) of the dark halo is responsible for the formation of the spiral structures in galactic disks, at least for some galaxies. We will restrict our consideration here to the gaseous disk. A separate study will be devoted to taking into account the stellar disk.

2. MODEL OF A GASEOUS DISK IN THE EXTERNAL POTENTIAL

The character of the spatial mass distribution in the dark halo determined from observations is uncertain. Several models for the halo density ϱ_h have been proposed, such as the models of Navarro et al. [30] (NFW) and Burkert [31], the exponential model [32], and the quasi-isothermal halo model [1, 33] (iso). We will generalize this last model for the case of a triaxial halo, by writing the following expression for the potential

$$\Psi_h(x,y,z) = 4\pi G\varrho_{h0}a_x^2 \times \left(\ln\xi + \frac{\arctan\xi}{\xi} + \frac{1}{2}\ln\frac{1+\xi^2}{\xi^2}\right), \quad (1)$$

where $\xi = \sqrt{\frac{x^2}{a_x^2} + \frac{y^2}{a_y^2} + \frac{z^2}{a_z^2}}$ and a_x, a_y, and a_z are characteristic scales along the corresponding axes. The Poisson equation gives the density distribution

$$\varrho_h(x,y,z) = \frac{\varrho_{h0}a_x^2}{\xi^2} \times \left[\left(\frac{1}{a_x^2} + \frac{1}{a_y^2} + \frac{1}{a_z^2}\right)\left(1 - \frac{\arctan\xi}{\xi}\right) - \frac{1}{\xi^2}\left(\frac{x^2}{a_x^4} + \frac{y^2}{a_y^4} + \frac{z^2}{a_z^4}\right) \times \left(2 + \frac{1}{1+\xi^2} - 3\frac{\arctan\xi}{\xi}\right)\right]. \quad (2)$$

In the limiting case of a centrally symmetric halo $a = a_x = a_y = a_z$, we have a quasi-isothermal model halo with the density distribution

$$\varrho(r) = \frac{\varrho_{h0}}{1 + (r/a)^2} \quad (3)$$

from (1), (2); this density distribution ensures constancy of the rotational velocity at large distances $r \gg a$, where the rotation curve has a plateau. The halo models differ in the circular velocity V_c at large distances ($r \gtrsim R_{\max}$, $R_{\max}$ is the boundary of the stellar disk) [34]. In the inner region of the galaxy, we have $V_c^{\rm iso} < V_c^{\rm Bur} < V_c^{\rm NWF}$ [34]. Therefore, other things being equal, our choice of the model (1) should be considered to yield a lower limit for the influence of the non-axisymmetric halo.

Below, we restrict our consideration to the model with $a_x \neq a_y = a_z$. If the halo is flattened in the vertical direction ($a_z < a_{x,y}$), this effectively increases the halo mass, since the gravitational force of the halo in the $z = 0$ plane becomes greater, so that the case $a_z = a_x$ again gives us a lower limit. When $q = a_x/a_y \neq 1$ in the plane of the disk, we have a non-axisymmetric halo that can, in general, rotate with a small angular velocity Ω_h. Observational data and cosmological models allow values $\varepsilon_h = |q - 1| \simeq 0$–$0.2$ [8–10].

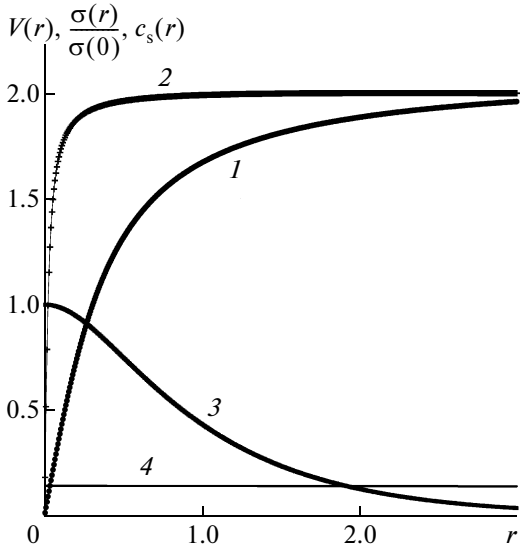

Fig. 1. Typical dependences of the (*1*, *2*) rotational velocity $V(r)$ (without and with a bulge, respectively), (*3*) surface density $\sigma(r)/\sigma(0)$, and (*4*) sound speed $c_s(r)$ on the radial coordinate for the initial equilibrium state of the gaseous disk.

Let us assume that the rotational angular velocity of the halo Ω_h is less than the rotational angular velocity of the outer edge of the disk, $\Omega(R) = V(R)/R$. If typical values of the linear velocity $V(R)$ for galactic disks in the plateau region are $V_{\max} \simeq$ 100–300 km/s at distances $R \simeq 10$–15 kpc ($\Omega(R) \sim$ 5–30 km s^{-1}kpc^{-1}), this implies for the angular velocity of the halo $\Omega_h \lesssim 5$ km s^{-1} kpc^{-1}.

Let us consider the complete system of gas-dynamical equations in the form

$$\frac{\partial \rho}{\partial t} + \nabla(\rho \mathbf{u}) = 0, \tag{4}$$

$$\frac{\partial \rho \mathbf{u}}{\partial t} + \nabla(\rho \mathbf{u}\mathbf{u}^T + P\hat{I}) = -\rho \nabla \Psi, \tag{5}$$

$$\frac{\partial E}{\partial t} + \nabla([E + P]\mathbf{u}) = -\rho \mathbf{u} \cdot \nabla \Psi, \tag{6}$$

where t is the time, ρ the gas density, P the pressure, $\mathbf{u} = [u, v, w]^T$ the velocity vector, $\hat{I} = \mathrm{diag}[1, 1, 1]$ a 3×3 unit tensor, and $\Psi = \Psi_0 + \Psi_g$ the gravitational potential, composed of an external component (halo + stellar disk) $\Psi_0(\mathbf{r}, t)$ and the potential of the self-gravitating gas $\Psi_g(\mathbf{r}, t)$. The total energy per unit volume of the gas is

$$E = \rho \left(e + \frac{\mathbf{u}^2}{2} \right), \tag{7}$$

where e is the specific internal energy. The equation of state of the gas is defined by $e = \dfrac{P}{\rho(\gamma - 1)}$, where γ is the adiabatic index. The system of equations (4)–(7) must be supplemented with the Poisson equation $\Delta \Psi_g = 4\pi G \varrho$, to take into account the self-gravity.

We used total variation diminishing (TVD) version of the MUSCL scheme [35, 36] to numerically model the system of gas-dynamical equations (4)–(6). We approximated the equations using the finite-volume method, which ensures that conservation laws are obeyed at the discrete level [37]. This numerical scheme is related to Godunov schemes with second-order accuracy in time and third-order in space. The modified HLLC method [38] was used to calculate the fluxes of physical quantities through cell boundaries; this provides a means to model shocks and contact and tangential discontinuities through the boundaries. The construction of the scheme with second-order accuracy in time was carried out using a predictor–corrector scheme compatible with the condition that the total variation of the numerical solution not decrease (the TVD condition [36]). A third-order approximation in space was used in regions of smooth flow, and was achieved using the MUSCL procedure for reconstructing simple quantities (the density, pressure, and velocity vector) at the boundaries of the computation cells. This simple and computationally efficient method makes it possible to obtain shocks spread over three cells. The corresponding parameter responsible for the artificial compression was used to improve the resolution of tangential and contact discontinuities in the interpolation.

The computations were carried out on cylindrical (r, φ, z) and Cartesian (x, y, z) grids with high resolution. The dimension of the numerical grids for the two-dimensional (2D) models reached 5000×5000 for the Cartesian grid and $(N_r \times N_\varphi) = 2400 \times 720$ for the polar grid. The grid parameters in the three-dimensional (3D) model were $N_r = 600, N_\varphi = 360, N_z = 200$. A special numerical algorithm was constructed for the through calculation of the gas–vacuum interface, which preserved the positivity of the scheme [39]. In this case, the matter is situated within the computation domain. A comparative analysis demonstrated the extremely small influence of the boundary conditions on the evolution of the constructed models for the gaseous disks.

In order to estimate the influence of the numerical technique used on the disk dynamics, we also carried out hydrodynamical calculations using Smoothed Particle Hydrodynamics (the SPH method) [40, 41]. The SPH algorithm is related to fully Lagrangian algorithms, and so is free of the need to use the approximation of a spatial grid; this removes a considerable number of theoretical and algorithmic difficulties. The scheme is constructed based on the motion of particles whose evolution in time and space directly reproduces the conservation of mass,

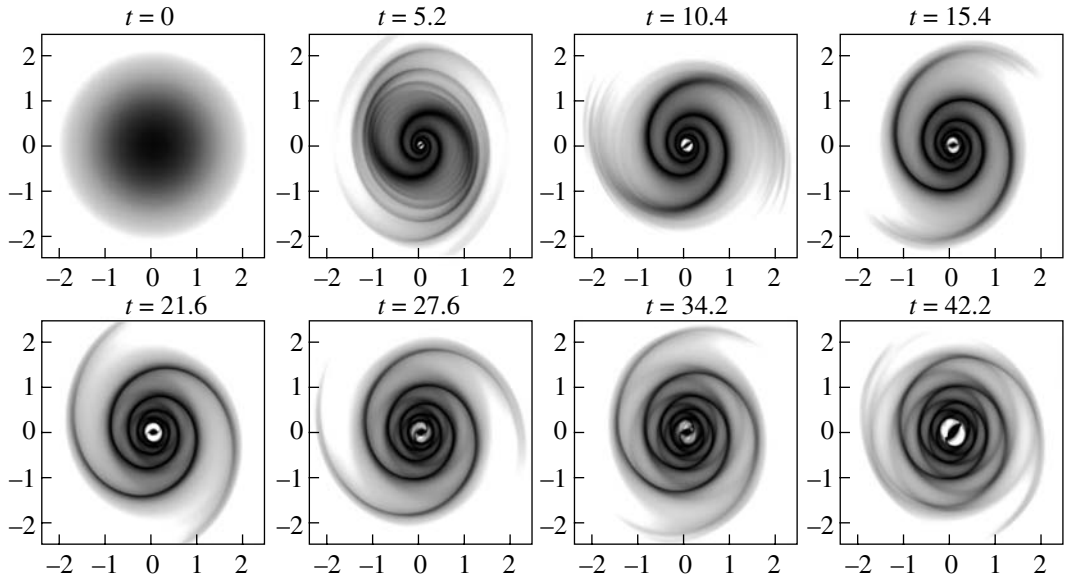

Fig. 2. Distributions of the logarithm of the surface density σ in the plane of the disk at various times, for the model with $d = 0.02$, $\varepsilon_h = 0.1$, $\mathcal{M}_0 = 10$, and $L_3 = 0.7$.

momentum, and angular momentum. A modification of the standard predictor–corrector scheme was used for the time integration of the SPH equations; this modification ensures second-order accuracy in time. The calculations were carried out $N = 10^5$–10^6 particles, and demonstrated good agreement with solutions based on the grid TVD method. The self-gravity was taken into account using the TREEcode algorithm.

The initial equilibrium state of the gaseous disk is defined by the radial and vertical profiles of the rotational velocity V, density ϱ, and sound speed c_s in the absence of radial and vertical motions, $u = w = 0$. It is convenient to characterize the state of the disk using the Mach number, $\mathcal{M} = V/c_s$. Since $\mathcal{M}$ depends on the coordinates, it is convenient to introduce the quantity $\mathcal{M}_0 = V_\mathrm{max}/c_s(r = 0)$. Figure 1 presents typical radial profiles of the disk parameters at the initial time for the assumed dimensionless quantities. The rotation curves are typical for galactic-disk components, and are characterized by a small section with a quasi-rigid-body rise at the disk center and a more extended section with roughly constant velocity (the so-called plateau in the rotation curve).

The numerical model assumes $G = 1$, and the galaxy mass within the limits of the radius $r \leq 1$ is $M_{gal} = 4$. The optical radius of the galaxy (the outer edge of the stellar disk) is $R = 2$ in dimensionless units. In this case, a typical value of the dimensionless rotational velocity of the disk is $V_\mathrm{max} \simeq 2$, and the rotational period of the periphery of the gaseous disk ($r \sim 2$–3) is $T \simeq 6$–10. The gaseous disk extends beyond R.

We considered various initial radial profiles of the gas surface density σ:

(1) $\sigma \propto \exp(-r/L)$,

(2) $\sigma \propto [1 + (r/L_1)^2 + (r/L_2)^6]^{-1}$,

(3) $\sigma \propto [1 + (r/L_3)^2]^{-5/2}$,

(4) $\sigma \propto \cosh^{-2}(r/L_4)$.

The calculation domains in the various models are situated within $R_\mathrm{max} = 5$–15, where $\sigma(R_\mathrm{max})/\sigma(0) = 10^{-5}$–$10^{-10}$, which ensures an absence of influence from boundaries.

At the initial time $t = 0$, the axisymmetric equilibrium disk is in the axisymmetric potential $\Psi(r, t = 0)$ with $\varepsilon_h = 0$ ($a_x = a_y$). Then, the value of the scale a_x was increased linearly to $\varepsilon_h = 0.001$–0.2 over a time τ_h for the various models. After the non-axisymmetry was "switched on" at times $t > \tau_h$, the halo potential remained constant.

In the following section, we describe the main results of our modeling of the disks, focusing on the possible generation of various structures by the triaxial halo, considering the morphology and kinematics of these structures based on the results of over 80 numerical experiments.

3. GASEOUS DISK IN A NON-AXISYMMETRIC HALO

The main free parameters of the constructed model and their typical dimensionless values are:

(1) the degree of non-axisymmetry of the halo $\varepsilon_h = 0$–0.2 ($q = a_y/a_x = 1 - \varepsilon_h$);

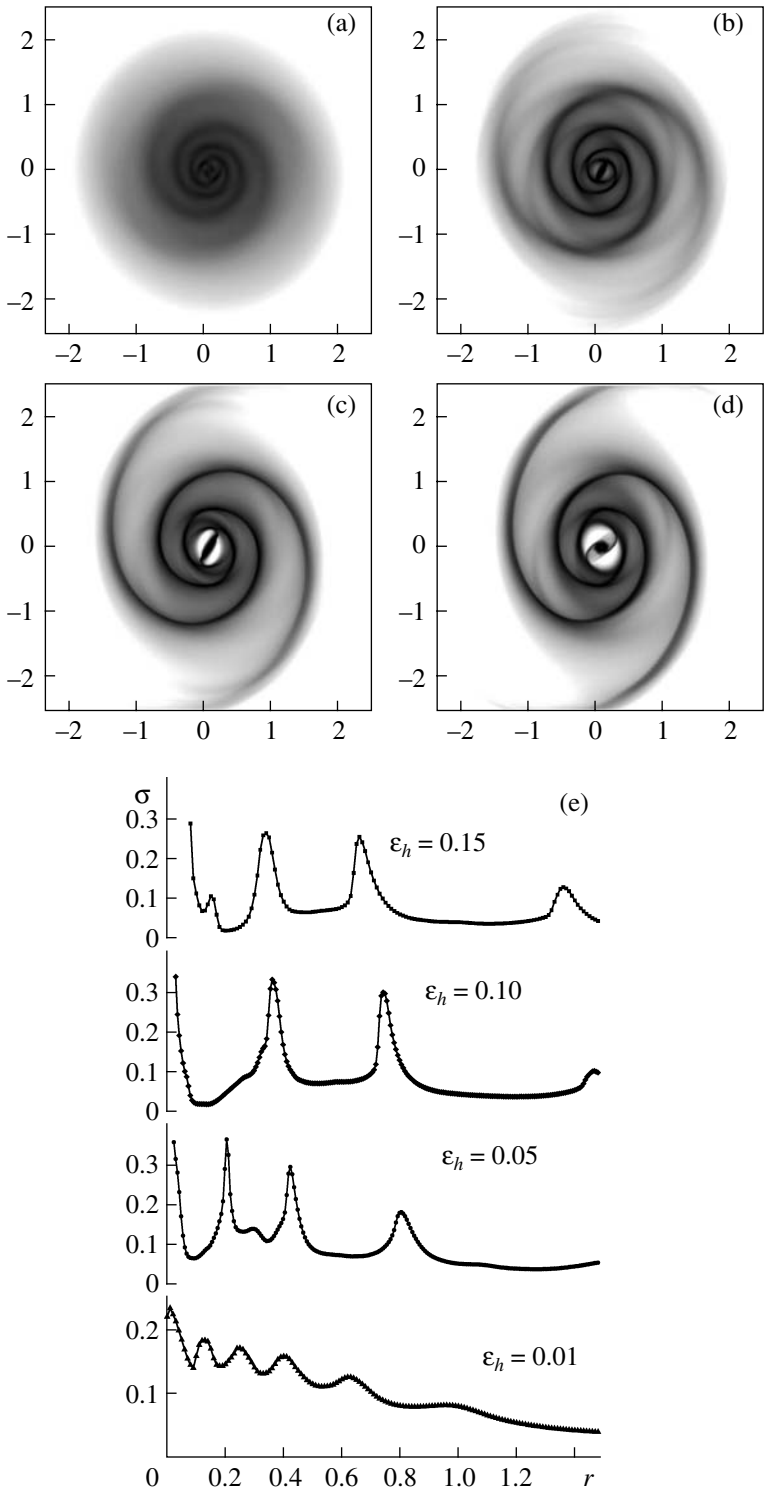

Fig. 3. Distributions of the logarithm of the surface density in the plane of the disk for models with $\mathcal{M}_0 = 10$, $d = 0.1$, and $\varepsilon_h =$ (a) 0.01, (b) 0.05, (c) 0.1, and (d) 0.15, all at the same time. (e) Radial profiles of the surface density for the fixed azimuth angle $\varphi = 0$ for the indicated ε_h values.

(2) the width of the quasi-rigid-body section of the rotational velocity in the central region of the disk $d = 0.015$–0.5;

(3) typical scales for the radial distribution of the surface density $L = 0.5$–1.5;

(4) the sound speed of the gas or the disk tem-

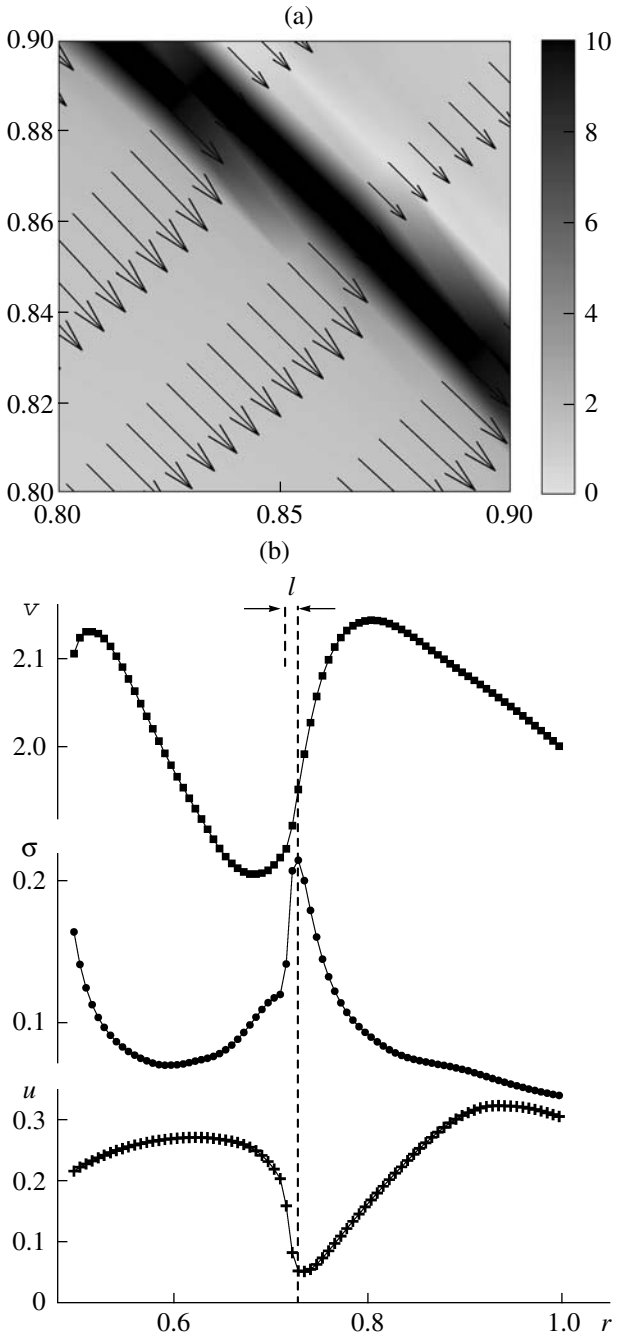

Fig. 4. Model with $\varepsilon_h = 0.1$, $d = 0.02$, $L_3 = 0.7$, $\mathcal{M}_0 = 10$, and $\Omega_h = 0$. (a) Distribution of $\log(\mathrm{div}\mathbf{u})^2$ (in shades of gray), together with the velocity field $\mathbf{u}$. (b) Radial profiles of the radial velocity u, azimuthal component v, and surface density σ near the spiral density wave. The function values at the nodes of the numerical grid are marked near the curves.

perature, characterized by the effective Mach number $\mathcal{M}_0 = 5$–30;

(5) the relative gas mass $\mu_g = M_g/M_0$ (M_0 is the galaxy mass within the radius $r \leq R = 2$);

(6) the rotational angular velocity of the halo $\Omega_h = 0$–0.2 corresponding to the corotation radius at the periphery of the gaseous disk;

(7) the transition time from the axisymmetric to the non-axisymmetric halo $\tau_h = 0$–30.

The character of the flow in the gaseous disk depends considerably on the values of the indicated model parameters. However, the generation of spiral structure is observed in all cases, and we have a long-lived, quasi-stationary, two-armed wave in the main

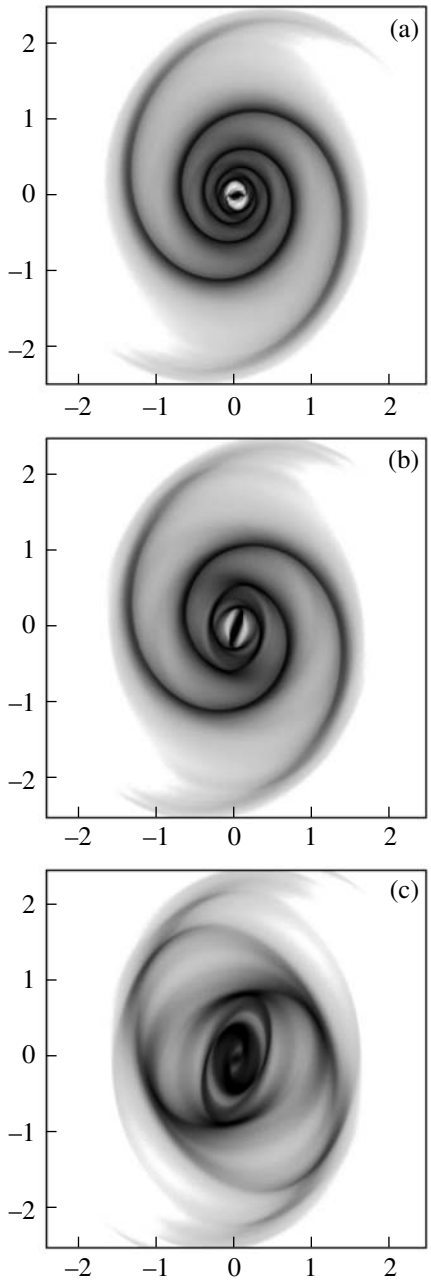

Fig. 5. Spiral patterns with various geometries in the central region at the same time for $\mathcal{M}_0 = 10$ and $\varepsilon = 0.1$, in the models with (a) $d = 0.02$, (b) 0.1, and (c) 0.3.

region of the disk ($0.5 \lesssim r \lesssim 2$). Figure 2 shows the typical long-term evolution of the disk ($t = 40$ corresponds to six rotations of the disk periphery $r \sim 2$). The two-armed perturbation covers almost the entire disk, and is trailing except at the center itself, where more complex structures are observed.

Let us note some typical features of the morphology and kinematics of the disk indicated by our numerical simulations:

1. In all cases, the presence of a non-axisymmetric halo leads to the formation of spiral structures in the gaseous disk (see the distribution of the logarithm of the surface density in Figs. 3a–3d). Under typical conditions, perturbations grow to the strongly nonlinear stage over one to three disk revolutions, forming a system of shocks (Fig. 3e). The time when the quasi-stationary spiral structure forms increases with decreasing ε_h. With decreasing ε_h, the spirals become more tightly wound and have smaller amplitudes, other conditions being equal (Fig. 3e). A massive, non-axisymmetric halo can generate nonlinear waves even when $\varepsilon_h < 0.01$, but the rise time in this case exceeds eight rotation periods of the disk periphery. The formation of the spiral structure in the essentially nonlinear stage depends only weakly on the time when the non-axisymmetric part of the potential is switched on, τ_h, which was varied from $\tau_h = 0$ (instantaneous) to an adiabatically slow ramping up during several rotations of the disk periphery (about 1–1.5 billion years for a typical S galaxy).

2. The analysis of the gas-flow structure indicates a complex character that includes a system of shocks and of regions of strong shear flows (Fig. 4). The nonlinear (shock) waves have large-scale structure, which encompasses the disk right to small densities $\varrho/\varrho_{\max} \sim 10^{-3}$. The shape of the spiral depends substantially on the model parameters, but it is a large-scale formation, formed by rotating through the angle of $\sim 2\pi$, or, in some cases, by more than 4π. The amplitude of the spiral waves depends on the degree of non-axisymmetry of the halo ε_h, but the formation of the shocks occurs for all of the parameter values considered. A zone of shear flow is formed in the region of the spiral density wave near the shock front (Fig. 4a). The region of strong variation of the tangential velocity component is large compared to the shock front, whose width ℓ is determined by the properties of the numerical model (Fig. 4b). The quantities σ and u exhibit a jump at the shock front (within ℓ), in contrast to v, whose region of variation is substantially larger than ℓ. The width of the shock front ℓ decreases with increasing resolution of the numerical scheme (increasing numbers of cells N_r, N_φ), so that the shock front is described by three to four numerical cells; this was achieved by using a numerical scheme with second-order of accuracy in time and third-order accuracy in the spatial coordinates. The width of the shear flow region is finite and does not depend on the choice of parameters for the numerical grid.

3. The geometry of the spiral patterns depends on the gas-rotation curve $V(r)$, the character of the density distribution in the dark halo $\varrho_h(r, \varphi)$, and the radial profiles of the disk surface density $\sigma(r)$ and the sound speed $c_s(r)$. Leading spirals, which always

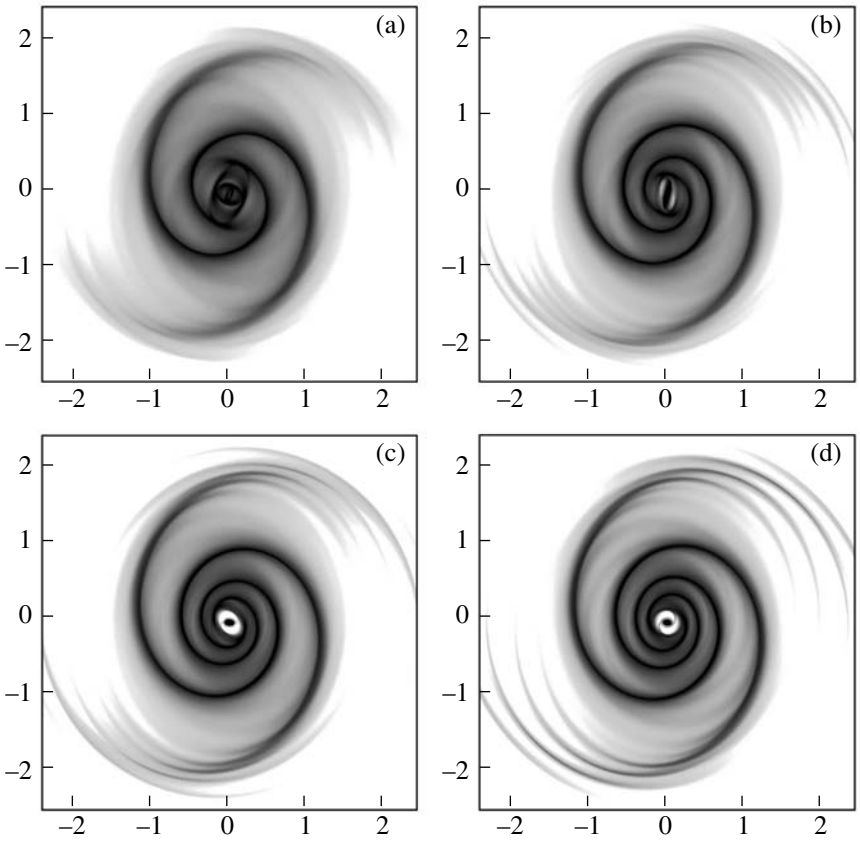

Fig. 6. Models with Mach numbers $\mathcal{M}_0 =$ (a) 10, (b) 15, (c) 20, and (d) 30 with $\varepsilon = 0.1$ and $d = 0.1$, all at the same time.

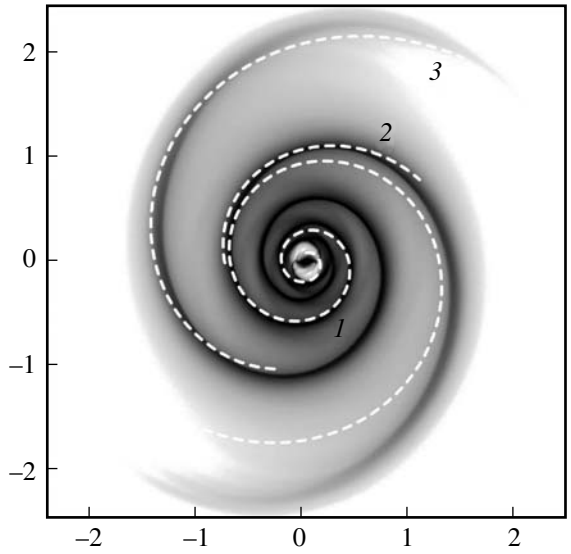

Fig. 7. Geometry of spirals in the model with $\mathcal{M}_0 = 10$, $\varepsilon_h = 0.1$, and $d = 0.02$. Superimposed on the distribution of the logarithm of the surface density are curves showing sections of logarithmic spirals with various pitch angles: (*1*) $i = 10^\circ$, (*2*) $i = 12^\circ$, and (*3*) $i = 14^\circ$.

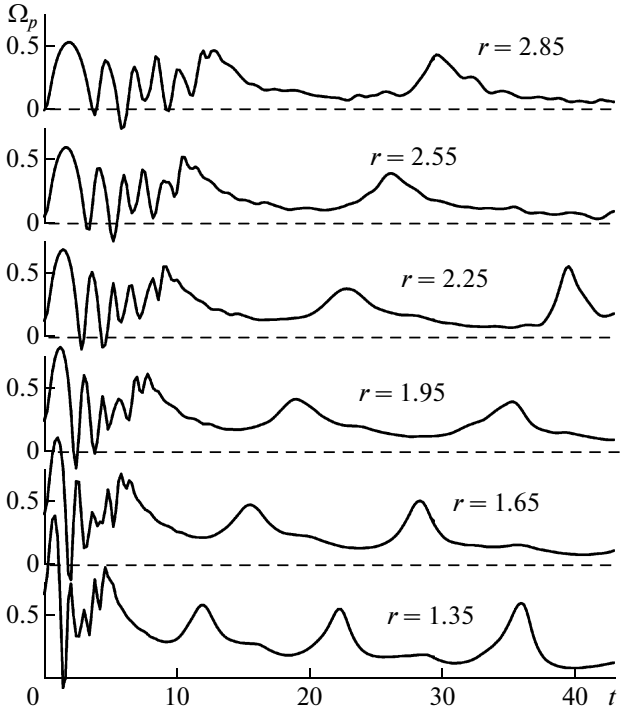

Fig. 8. Dependences $\Omega_p(t)$ for the two-armed spiral for disk rings situated at different distances from the center r.

become trailing spirals at the periphery and produce complex Θ structures (embedded Θ structures are possible) at the center, can be formed in the central part of the disk (Fig. 5). In all the figures presented here, the gaseous disk rotates in the counterclockwise direction. Thus, trailing spirals untwist in the clockwise direction, and leading spirals in the counterclockwise direction. The presence of leading spirals in the very central zone of the disk is clearly visible in Figs. 3d, 5c and Figs. 9a, 9b, 10a.

4. The generation of pronounced Θ structures formed by leading spirals in the central region occurs in gaseous disk models without allowance for the perturbation of the stellar-subsystem's density. Since Θ structures are not formed in models with collisionless stellar disks, the central Θ structures will be weaker in self-consistent stellar-gaseous systems, and the question of the dynamics of the central region requires a separate study. Note that complex gaseous structures manifest as, e.g., dust streaks inside the bar are clearly visible in images of SB galaxies (e.g., NGC 1672, NGC 1300, NGC 1365, NGC 3627, etc.). In addition to gaseous–dusty spirals emerging from the center, on the whole, along the major axis, structures tracing the shape of the bar itself (e.g., in galaxies NGC 1097, NGC 1288, NGC 2903) or outer spiral arms that do not start from the bar ends but encompass part of the leading edge of the bar (NGC 4548,VCC 1615) are observed. The so-called three-kpc arms in our Galaxy may serve as an example.

5. As in the case of decreasing ε_h, decreasing the zone of the quasi-rigid-body rotation in the center of the gaseous disk promotes the formation of more tightly wound spirals. Simultaneously, the conditions for the generation of Θ structures in the center become less favorable. Trailing spirals now arise in the center itself and encompass the entire disk (Fig. 5).

6. In cooler disks (with higher Mach numbers), more tightly wound and thinner spirals are formed in the nonlinear stage (Fig. 6).

7. The typical spiral pitch angles are $i \simeq 5°–20°$. More open patterns do not form in the models considered. Figure 7 shows an example of an approximation of the obtained structure with sections of logarithmic spirals $r = r_a \exp(\chi\varphi)$ with pitch angles $i = \pi/2 - \arccos(\chi/\sqrt{1+\chi^2})$. For the case presented, i increases from 10° in the central zone to 14° at the periphery. This small increase in i with radius is typical for the models constructed.

8. Let us now consider the rotational angular velocity of the spiral pattern Ω_p. Figure 8 shows the time dependences of Ω_p for the two-armed spiral at various radii r. An initial stage in the pattern formation can be distinguished ($t \lesssim 10$; these processes proceed faster nearer the center than at the periphery), after which

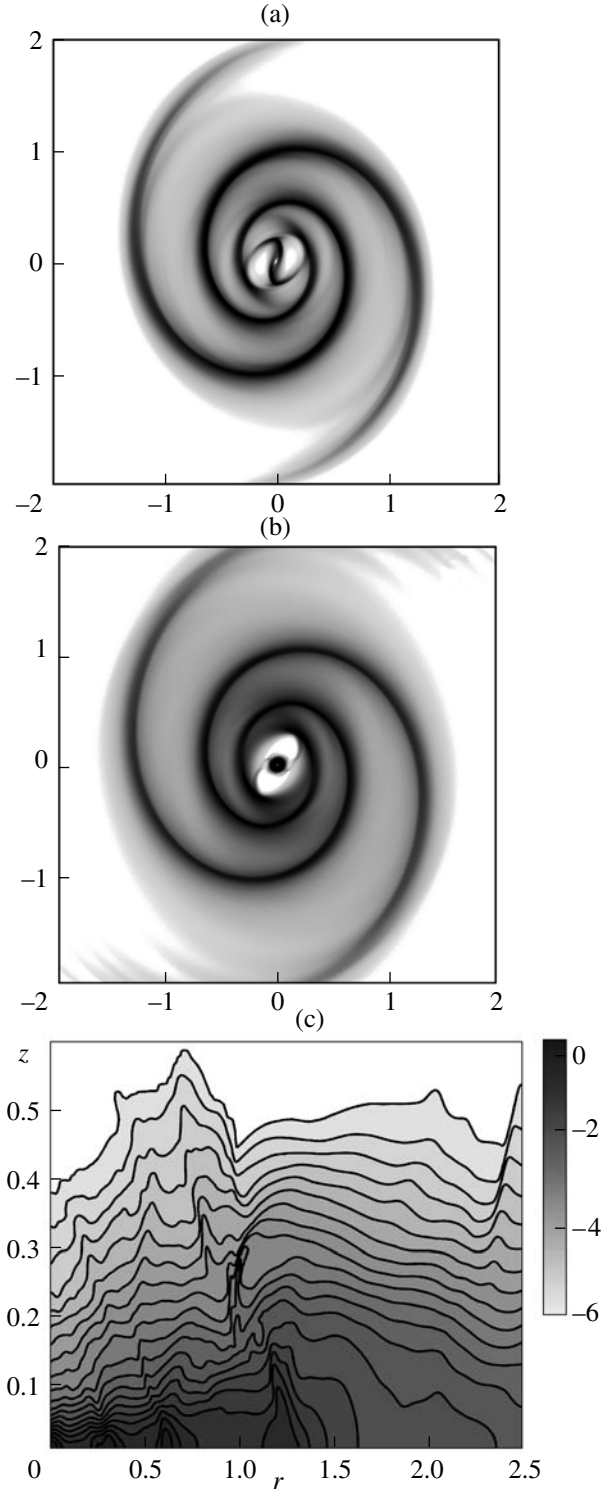

Fig. 9. Distributions of the surface density in the (a) 3D and (b) 2D models in the TVD computations for $\varepsilon_h = 0.1$, $\mathcal{M}_0 = 15$, and $d = 0.125$, and (c) the vertical structure of the volume density in the $(x, 0, z)$ plane for the azimuth angle $\varphi = 0$.

a quasi-periodic rotation regime for the non-linear perturbations develops. We emphasize that the spiral pattern rotates even in the case of a stationary halo $\Omega_h = 0$. However, the rotational angular velocity is then low, and the corresponding corotation radius is beyond the disk. Computations with a slowly rotating halo, $\Omega_h \lesssim 0.2$, show that the geometry and kinematics of the spiral patterns depend weakly on

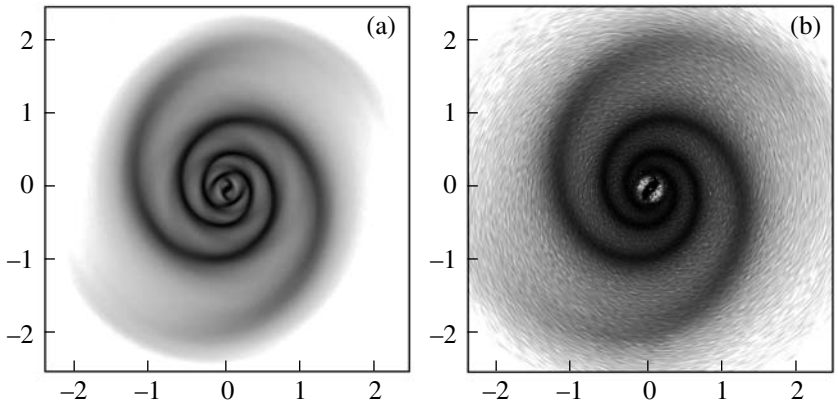

Fig. 10. Example of a comparison of the spiral structure of the (a) 2D TVD model and (b) the 3D SPH computation.

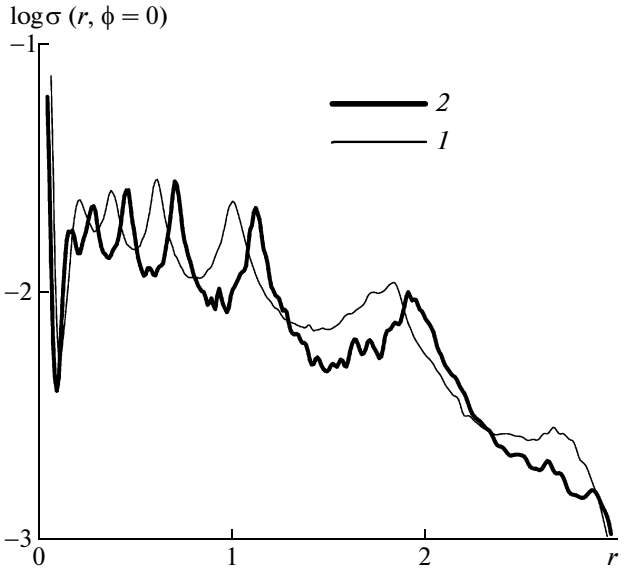

Fig. 11. Radial profiles of the surface density along the ray $\varphi = 0$ in the SPH disk model (*1*) without and (*2*) with self-gravity.

Ω_h. A small increase of the angular velocity of the wave in the disk is observed with increasing. Ω_h[1] Objects whose spiral structure rotates fairly slowly and whose corotation radius is at the periphery of, or even outside, the outer limits of the spiral structure (e.g., in NGC 3359 [42]) are of interest for the spiral-structure formation mechanism discussed here.

9. There is qualitative agreement between the results of the 2D and 3D gas-dynamical computations (Figs. 9, 10). In the initial stages of formation of the spiral pattern (over several rotations), the formation of strongly nonlinear wave fronts propagating in the vertical direction at an angle to the plane of the gaseous disk is observed. The geometry of the trailing spiral pattern in the main part of the disk differs slightly in the 2D and 3D models (Figs. 9, 10). Discrepancies are observed only in the central region, where the formation of complex, small-scale structures is possible. In this case, the presence of a vertical dimension can substantially change the gas dynamics, since the sound speed in the center is known not to be small compared to the rotational velocity of the system, and vertical motions are of considerable importance [43].

10. On the whole, taking self-gravity into account increases the efficiency of the formation of the spiral pattern by the non-axisymmetric halo. We have con-

[1] Note that the question of the location of the corotation radius is far from resolved, and this is one of the key questions in spiral structure theory.

sidered only gravitationally stable disks. A change of the wave geometry is observed, and the wave amplitude increases (Fig. 11).

In conclusion, let us summarize the main differences of the spiral-pattern modeling in a non-axisymmetric halo and in the presence of a central bar:

(1) the bar is a rapidly rotating structure relative to the spiral pattern;

(2) the dimensions of the central stellar bar are small compared to those of the galactic disk, and the effect of the bar is dominant at the center and rapidly decreases with radius; the triaxial halo influences the entire disk, and influences the disk center only to a smaller degree;

(3) the degree of non-axisymmetry of the halo is substantially less than of that the bar, so that the geometry of the spiral waves differs considerably from the disk in the nonaxisymmetric halo, even inside the bar, where the gas, on average, rotates faster than the bar.

The results of our numerical modeling show that a triaxial (non-axisymmetric in the plane of the disk) halo can lead to the generation of a spiral pattern in the galactic disk, whose properties depend strongly on the parameters of the disk and halo.

The question of whether non-axisymmetric halos are responsible for the real spiral patterns observed in galaxies is, of course, far from being resolved. The real picture can be made considerably more complex by the formation of transient spirals, a central stellar bar, or global modes [44] due to the development of gravitational instability. In any case, the models considered here can be used to place some constraints on the shapes of dark halos in the plane of their galactic disks. If the properties of the observed spiral pattern in a galaxy are incompatible with our modeling results, then this indicates a high degree of axisymmetry for the dark halo in the plane of the disk.

ACKNOWLEDGMENTS

The authors thank A.V. Zasov and V.I. Korchagin for numerous discussions. The numerical computations were performed on the SKIF MSU "Chebyshev" supercomputer with the assistance of A.V. Zasov and N.V. Tyurina. This work was supported by the Russian Foundation for Basic Research (projects 07-02-01204, 09-02-97021), "Dynasty" Foundation, and the Federal Targeted Program "Scientific and Scientific–Pedagogical Staff of Innovative Russia" [grant 2009NK-21(7)].

REFERENCES

1. A. V. Khoperskov, A. V. Zasov, and N. V. Tyurina, Astron. Rep. **47**, 357 (2003).
2. A. V. Zasov, A. V. Khoperskov, and N. V. Tyurina, Astron. Lett. **30**, 593 (2004).
3. A. V. Khoperskov, A. V. Zasov, and N. V. Tyurina, Astron. Rep. **45**, 180 (2001).
4. A. Khoperskov, D. Bizyaev, N. Tiurina, and M. Butenko, Astron. Nachr. **331**, 731 (2010).
5. A. V. Zasov and O. K. Sil'chenko, Phys. Usp. **53**, 415 (2010).
6. I. D. Karachentsev, O. G. Kashibadze, D. I. Makarov, and R. B. Tully, Mon. Not. R. Astron. Soc. **393**, 1265 (2009).
7. A. V. Khoperskov and N. V. Tyurina, Astron. Rep. **47**, 443 (2003).
8. A. R. Zentner, A. V. Kravtsov, O. Y. Gnedin, and A. A. Klypin, Astrophys. J. **629**, 219 (2005).
9. J. S. Bullock, in *The Shapes of Galaxies and Their Dark Halos, Proceedings of the Yale Cosmology Workshop, May 28–30, 2001, New Haven, Connecticut, USA,* Ed. by P. Natarajan (World Scientific, Singapore, 2002), p. 109.
10. J. Bailin and M. Steinmetz, Astrophys. J. **627**, 647 (2005).
11. K. V. Johnston, D. R. Law, and S. R. Majewski, Astrophys. J. **619**, 800 (2005).
12. A. Helmi, Mon. Not. R. Astron. Soc. **351**, 643 (2004).
13. S. C. Keller, S. Murphy, S. Prior, et al., Astrophys. J. **678**, 851 (2008).
14. R. Ibata, M. Irwin, and G. Lewis, Nature **412**, 49 (2001).
15. Z. Shang, Z. Zheng, E. Brinks, et al., Astrophys. J. **504**, L23 (1998).
16. E. H. Wehner, J. S. Gallagher, P. Papaderos, et al., Mon. Not. R. Astron. Soc. **371**, 1047 (2006).
17. A. Gualandris and S. P. Zwart, Mon. Not. R. Astron. Soc. **376L**, 29 (2007).
18. Q. Yu and P. Madau, Mon. Not. R. Astron. Soc. **379**, 1293 (2007).
19. O. Y. Gnedin, A. Gould, J. Miranda-Escude, and A. Zentner, Astrophys. J. **634**, 344 (2005).
20. S. Zibetti, S. White, and J. Brinkmann, Mon. Not. R. Astron. Soc. **347**, 556 (2004).
21. M. G. Abadi, J. F. Navarro, and M. Steinmetz, Mon. Not. R. Astron. Soc. **365**, 747 (2006).
22. R. P. Olling and M. R. Merrifield, Mon. Not. R. Astron. Soc. **311**, 361 (2000).
23. H. L. Morrison, A. Helmi, J. Sun, et al., Astrophys. J. **694**, 130 (2009).
24. S. E. Koposov, H.-W. Rix, and D. W. Hogg, Astrophys. J. **712**, 260 (2010).
25. A. A. Abdo, M. Ackermann, and M. Ajello, arXiv:1002.4415 [astro-ph.CO] (2010).
26. A. V. Zasov, A. V. Moiseev, A. V. Khoperskov, and E. A. Sidorova, Astron. Rep. **19**, 79 (2008).
27. A. V. Khoperskov, M. A. Eremin, S. S. Khrapov, and A. G. Morozov, Vestn. Volgogr. Gos. Univ., Ser. Mat. Fiz. **11**, 100 (2007–2008).
28. K. Bekki and K. Freeman, Astrophys. J. **574**, 21 (2002).

29. A. V. Tutukov and A. V. Fedorova, Astron. Rep. **50**, 785 (2006).
30. J. F. Navarro, C. S. Frenk, and S. White, Astrophys. J. **490**, 493 (1997).
31. A. Burkert, Astrophys. J. **447L**, 25 (1995).
32. R. Fux, Astron. Astrophys. **327**, 983 (1997).
33. K. G. Begeman, A. H. Broeils, and R. H. Sanders, Mon. Not. R. Astron. Soc. **249**, 523 (1991).
34. Y. Sofue, Publ. Astro. Soc. Jpn. **61**, 153 (2009).
35. B. van Leer, J. Comput. Phys. **32**, 101 (1979).
36. A. Harten, J. Comput. Phys. **49**, 357 (1983).
37. A. G. Kulikovskii, N. V. Pogorelov, and A. Yu. Semenov, *Mathematical Aspects of Numerical Solution of Hyperbolic Systems* (Fizmatlit, Moscow, 2001; Chapman and Hall, CRC, Boca Raton, 2000).
38. S. Li, J. Comput. Phys. **203**, 344 (2004).
39. M. A. Eremin, A. V. Khoperskov, and S. A. Khoperskov, Izv. Volgogr. Gos. Tekhn. Univ. **6** (8), 24 (2010).
40. J. J. Monaghan, Ann. Rev. Astron. Astrophys. **30**, 543 (1992).
41. D. J. Price and J. J. Honaghan, Mon. Not. R. Astron. Soc. **374**, 1347 (2007).
42. P. A. Patsis, D. E. Kaufmann, S. T. Gottesman, and V. Boonyasait, Mon. Not. R. Astron. Soc. **394**, 142 (2009).
43. N. N. Gorkavyi and A. M. Fridman, *Physics of Planetary Rings* (Nauka, Moscow, 1994; Springer, New York, 1999).
44. V. Korchagin, N. Kikuchi, S. M. Miyama, et al., Astrophys. J. **541**, 565 (2000).

Translated by O. Merkulova